Available online at www.sciencedirect.com
ScienceDirect
Trans. Nonferrous Met. Soc. China 30(2020) 1511−1523
Transactions of Nonferrous Metals Society of China
www.tnmsc.cn

Effect of Cu on microstructure, mechanical properties, and texture evolution of ZK60 alloy fabricated by hot extrusion−shearing process

Shuai DAI[1,2], Feng WANG[1,2], Zhi WANG[1,2], Zheng LIU[1,2], Ping-li MAO[1,2]

1. School of Materials Science and Engineering, Shenyang University of Technology, Shenyang 110870, China;
2. Key Laboratory of Magnesium Alloys and the Processing Technology of Liaoning Province, Shenyang 110870, China

Received 13 September 2019; accepted 20 April 2020

Abstract: As-cast Mg−6Zn−*x*Cu−0.6Zr (*x*=0, 0.5, 1.0, wt.%) alloys were fabricated by permanent mold casting; then, the alloys were subjected to homogenization heat treatment and extrusion−shearing (ES) process. The microstructure and mechanical properties of the alloys were evaluated by OM, SEM/EDS, XRD, TEM, EBSD and tensile tests. The results show that the hard MgZnCu phase in Cu-added alloy can strengthen particle-stimulated nucleation (PSN) effect and hinder the migration of dynamic recrystallization (DRX) grain boundary at an elevated temperature during ES. The ZK60+0.5Cu alloy shows an optimal tensile strength–ductility combination (UTS of 396 MPa, YS of 313 MPa, and δ=20.3%) owing to strong grain boundary strengthening and improvement of Schmid factor for $\{0001\}\langle 11\bar{2}0\rangle$ basal slip. The aggregation of microvoids around the MgZnCu phase mainly accounts for the lower tensile elongation of ZK60+1.0Cu alloy compared with ZK60 alloy.

Key words: Mg−Zn−Cu−Zr alloy; extrusion−shearing process; microstructure characterization; mechanical properties; texture evolution; strengthening mechanism

1 Introduction

Magnesium (Mg) alloys are desirable candidates as the lightest structural materials in aerospace and automotive industries owing to their low density and high specific strength [1,2]. However, for as-cast Mg alloy, insufficient mechanical properties severely restrict widespread applications of alloy [3,4]. Several studies have clarified the possible effect of hot deformation and microalloying on microstructural evolution and strength of Mg alloy [5−7]. Trace addition of rare earth (RE) elements is essential to improve the microstructure and mechanical properties of extruded Mg−Zn−Zr alloys, such as Y [8], Er [9], Ce [10] and Yb [11]. Among these RE elements, addition of Y can effectively act as a heterogeneous nucleation site of α-Mg based on the lattice match theory because of the same hcp structures and similar lattice parameters between Y and Mg atoms, thus enabling the strong grain refining effect on the as-cast alloy. The particles with predominant thermal stability formed in the billet during casting can induce strong particle-stimulated nucleation (PSN) during hot plastic deformation; for example, addition of Sn [12], Ca [13] and Al [14] enables the formation of hard second phases coexisting with α-Mg matrix (e.g., Mg_2Sn, Mg_2Ca and $Mg_{17}Al_{12}$ phases). Interestingly, the Ca element even weakens

Foundation item: Project (XLYC1807021) supported by Liaoning Revitalization Talents Program, China; Project (2019JH3/30100014) supported by Joint Research Fund of Lianning-Shenyang National Laboratory for Materials Science, China; Project supported by Liaoning BaiQianWan Talents Program, China; Project (RC200414) supported by Innovation Talent Program in Sciences and Technologies for Young and Middle-aged Scientists of Shenyang City, China; Project (XLYC1908006) supported by High Level Innovation Team of Liaoning Province, China

Corresponding author: Feng WANG; Tel: +86-15002424621; E-mail: wf9709@126.com

DOI: 10.1016/S1003-6326(20)65315-8

the basal texture in a similar manner as RE elements. The Al element favors the precipitation of massive nanosized Mg_2Sn precipitates in the Mg−1Zn−4Al−7Sn (wt.%) alloy system, introducing strong precipitation strengthening, and the corresponding mechanical properties show a slight increase compared with Al-free alloy. Previous studies have confirmed that the addition of Cu could significantly increase the eutectic temperature and improve the castability of Mg–Zn alloys [15,16], and it is reasonable to subject Mg–Zn–Cu alloy to a higher solution treatment temperature. More recently, Cu is proven to be the most effective element to improve the age-hardening response of ZK60; the addition of 0.5 wt.% Cu results in a significant improvement of tensile properties after an isothermal ageing at 180 °C [17]. Additionally, the ternary MgZnCu phase can be observed with the Cu addition, which is a Laves phase of C15 $MgCu_2$ type with a high melting point and superior thermal stability [18]. Herein, underlying PSN mechanism can be inferred in the Mg–Zn–Cu alloy system during plastic deformation. The electromagnetic interference (EMI) and shielding effectiveness (SE) significantly increase with increasing Cu content of extruded alloy [19]. Notably, the addition of Cu with a large atomic radius can increase the lattice parameter of Mg doped via first-principles calculations, and the *c/a* ratio of Mg decreases, which makes the prismatic planes {1010} have the same close-packing degree as the basal plane (0001) [20]. Therefore, the activation of prismatic slip system facilitates severe plastic deformation of Mg alloys.

In equal channel angular pressing (ECAP), activation of extra shear forces in die corner is beneficial to obtaining fully DRX grain structures via rotating coarse unDRX grains while weakening the basal texture intensity [21]. Except for the extrusion process parameters such as temperature, ram speed and extrusion ratio, the ECAP route is a dominating factor in the formability of Mg alloy [22−24]. Multipass ECAP can be successfully achieved along the *Bc* route, i.e., the longitudinal axis of samples is rotated by 90° between two passes. The alloy with superior ductility is commonly conducted on *Bc* route, because an increase in Schmid factor for $\{10\bar{1}0\}\langle 11\bar{2}0\rangle$ pyramidal slip favors the activation of the slip system [25]. In addition, the external angle of die corner cannot be ignored. The bimodal structure consisting of DRX grains with a diameter of 2.4 μm and unDRX grains with a diameter of 10.9 μm is obtained as the ZK60 alloy subjected to four-pass ECAP owing to insufficient shear forces induced by a low external angle of 37° [26]. A novel plastic deformation including the initial forward extrusion and subsequent shearing process (ES) is proposed in the three-dimensional finite element (3D FEM) simulation, which can improve equivalent strain and volume fraction of DRX grains [27].

A novel ES steel die with an extrusion ratio of 11.56, an internal angle between two channels of 90°, and an external angle of 0°, can avoid cracking of samples under sufficient equivalent strain provided. In this study, the effect of Cu addition on the microstructural evolution and mechanical properties of ES ZK60 alloy was evaluated. The strengthening mechanism was also elucidated to facilitate the application of ES Mg−Zn−Cu−Zr alloys.

2 Experimental

As-cast Mg−6Zn−*x*Cu−0.6Zr (*x*=0, 0.5, 1.0, wt.%) alloys were prepared from high-purity Mg, Zn and Cu (99.95%), and Mg−30Zr (wt.%) master alloys. First, pure Mg was melted at 700 °C in an electric resistance furnace under a protective gas mixture of 99.5% N_2 and 0.5% SF_6 (vol.%). The Zn, Cu and Mg−30Zr master alloys were added to pure Mg melt after ~1.5 h, and the melting temperature was increased to 720 °C. The temperature was maintained at 720 °C for 30 min to ensure that the alloying elements were completely dissolved. Subsequently, the melts were cooled to 700 °C and poured into a preheated metal mold (*d*75 mm × 75 mm). Inductively coupled plasma mass spectrometry (ICP-AES) was used to confirm the chemical compositions of as-cast billets, and the corresponding results are given in Table 1. Billets with a dimension of *d*68 mm × 68 mm were machined from the ingot, and homogenization treatment was performed at 400 °C for 20 h for Cu-added alloys and 380 °C for 15 h for Cu-free alloy (T4). Water quenching was performed to obtain a supersaturated solid solution favorable for the subsequent ES process. The ingots were extruded into bars of 20 mm in diameter at 400 °C under an extrusion ratio of 11.56 and an extrusion

speed of 40 mm/min. The detailed schematic illustrations of the ES dies and samples are shown in Fig. 1.

Table 1 Chemical composition of alloys (wt.%)

Alloy	Zn	Cu	Zr	Mg
ZK60	5.9	−	0.63	Bal.
ZK60+0.5Cu	6.1	0.48	0.60	Bal.
ZK60+1.0Cu	6.0	1.01	0.58	Bal.

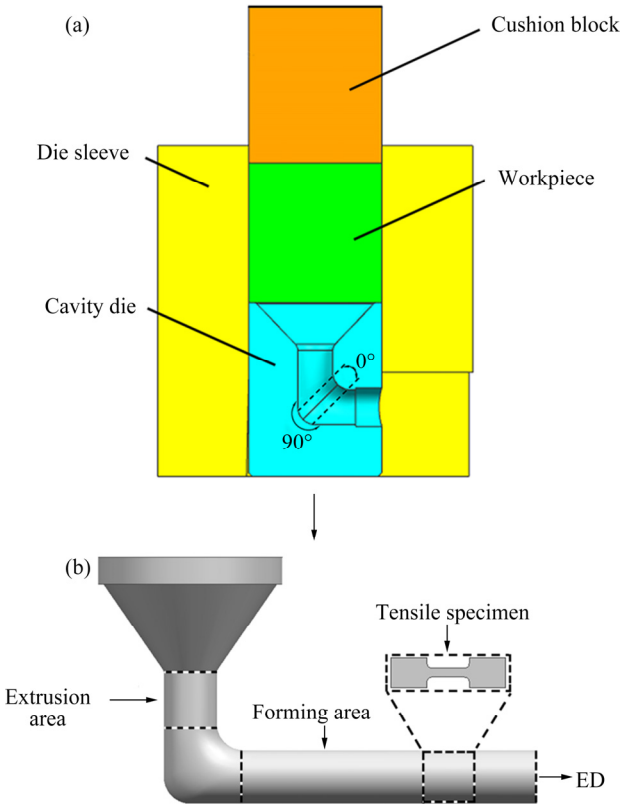

Fig. 1 Schematic illustrations of ES die (a) and ES sample model (b)

The as-cast and as-homogenized samples for microstructure observation were polished and etched with 4 vol.% nitrate alcohol solution, while the as-extruded samples were etched with glacial acetic acid containing 40 mL alcohol, 5 mL acetic acid, 3 g picric acid, and 5 mL distilled water. The microstructural evolution and phase analysis were performed using a Zeiss Axio Observer A1 optical microscope (OM), Hitachi S−3400N scanning electron microscope (SEM) equipped with an energy-dispersive X-ray spectrometer (EDS), D/max III A X-ray diffractometer (XRD), and JEM−2100 transmission electron microscope (TEM) operating at 200 kV. For TEM imaging, disk-shaped specimens with a thickness of 50 μm and a diameter of 3 mm were fabricated via the metallographic technique. Then, the disk-shaped specimens were placed in a 3.5 kV Gatan 691 ion beam at 4° until a pinhole appeared near the center. Electron backscattered diffraction (EBSD) analysis was conducted using a Gemini SEM 300 equipped with an HKL-EBSD system operating at 15 kV with a step size of 0.2 μm. The EBSD samples were mechanically and electrochemically polished in an electrolyte composed of 10% perchloric acid and 90% ethanol at 10 V and −30 °C for 60 s. Tensile samples with a gauge length of 10 mm and a thickness of 2 mm were obtained from the forming area in the ES bar using an electric spark machine. Tensile tests were performed at ambient temperature using a WDW−100 universal testing machine at an initial strain rate of 1×10^{-3} s^{-1} with load direction parallel to extrusion direction (ED).

3 Results and discussion

3.1 Microstructural characteristics of as-cast and as-homogenized alloys

The microstructures of as-cast alloys are shown in Fig. 2. Further grain refinement is achieved with Cu addition. With Cu addition, the amount of globular-shaped particles within grain interiors decreases. Additionally, the morphology of stripe-shaped particles along grain boundary changes from a discontinuous dendritic structure into a continuous network, and apparent grain boundary coarsening is observed (Figs. 2(a, c, e)). The results of EDS analysis (Table 2) show that the globular-shaped and short stripe-shaped particles are both $MgZn_2$ phases in the Cu-free alloy (Fig. 2). A certain amount of globular-shaped $MgZn_2$ phases observed within grain interiors can be ascribed to solidification and precipitation during casting, consistent with previous results in Mg−Zn alloy systems [28−30]. The coarse elongated MgZnCu phases are clearly observed in Cu-added alloys, with the size and fraction both gradually increasing with increasing Cu addition, but it is opposite for $MgZn_2$ phases (Figs. 2(b, d, f)). Therein, the typical fishbone-shaped MgZnCu phases are dominant in ZK60+1.0Cu alloy (Fig. 2(f)).

The microstructures of as-homogenized alloys are shown in Fig. 3. Most intermetallics are

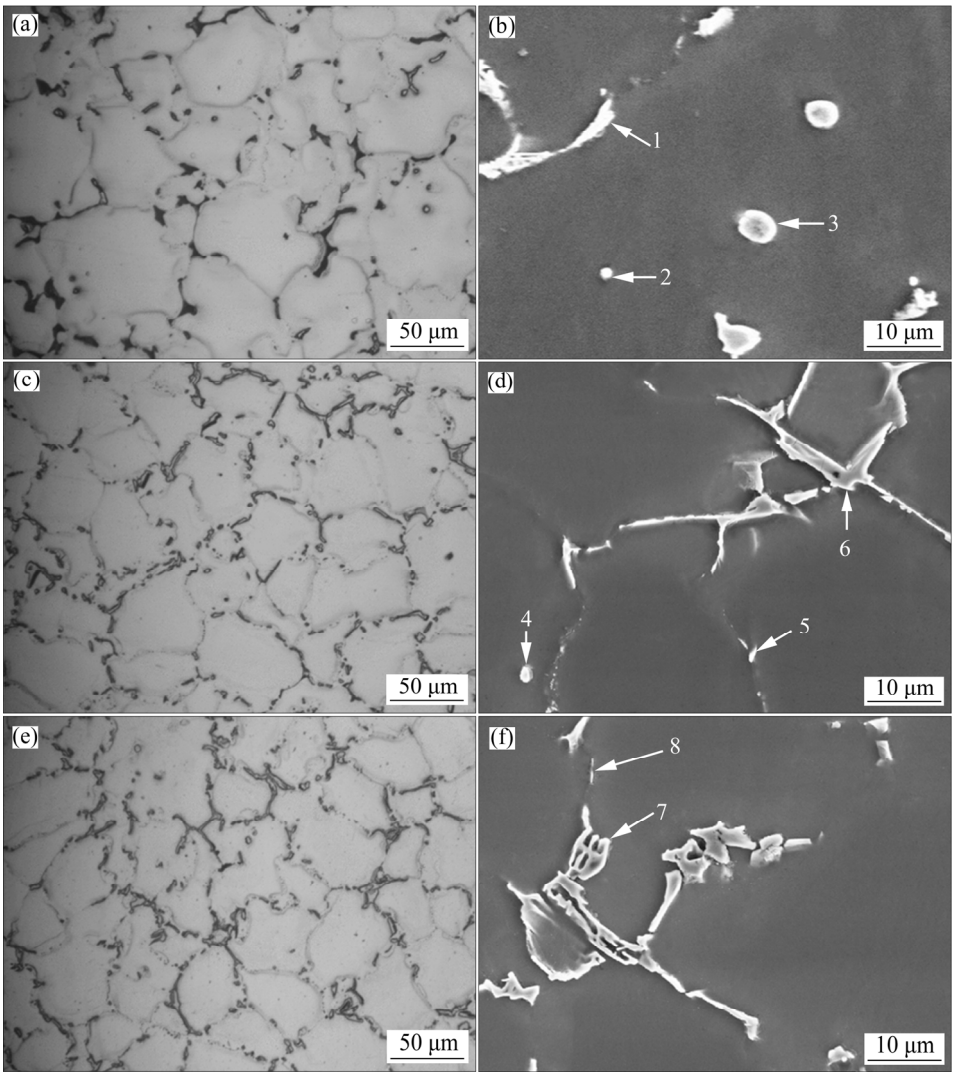

Fig. 2 Optical microstructures (a, c, e) and SEM images (b, d, f) of as-cast ZK60 (a, b), ZK60+0.5Cu (c, d) and ZK60+1.0Cu (e, f) alloys

Table 2 EDS results of phases shown in Fig. 2

Position	Content/at.%			Possible phase
	Mg	Zn	Cu	
1	45.68	54.32	−	$MgZn_2$
2	30.74	69.26	−	$MgZn_2$
3	48.41	51.59	−	$MgZn_2$
4	42.13	57.87	−	$MgZn_2$
5	51.45	48.55	−	$MgZn_2$
6	46.14	15.45	38.41	MgZnCu
7	23.09	29.39	47.53	MgZnCu
8	57.43	42.57	−	$MgZn_2$

dissolved into α-Mg matrix, and grain boundaries become unclear after solid solution treatment (Figs. 3(a–c)), particularly for ZK60 alloy (Fig. 3(a)). In the Cu-added alloy, the volume fraction of residual particles in α-Mg matrix increases with increasing Cu content (Figs. 3(b, c)). The EDS elemental mappings show that the residual particles mainly contain Cu and Zn of ZK60+1.0Cu alloy (Figs. 3(d–f)), which can be considered to be MgZnCu and $MgZn_2$ phases. Because the $MgZn_2$ phase has hp12 crystal structure with poor thermal stability [31], it is not surprising that substantial $MgZn_2$ phase is dissolved into α-Mg matrix.

Figure 4 shows the XRD patterns of as-cast and as-homogenized alloys. In the as-cast alloys, the XRD pattern of Cu-free alloy includes peaks of α-Mg and $MgZn_2$ phases, while the XRD pattern of Cu-added alloys shows extra peaks of MgZnCu phase (Fig. 4(a)). The peak intensity of MgZnCu

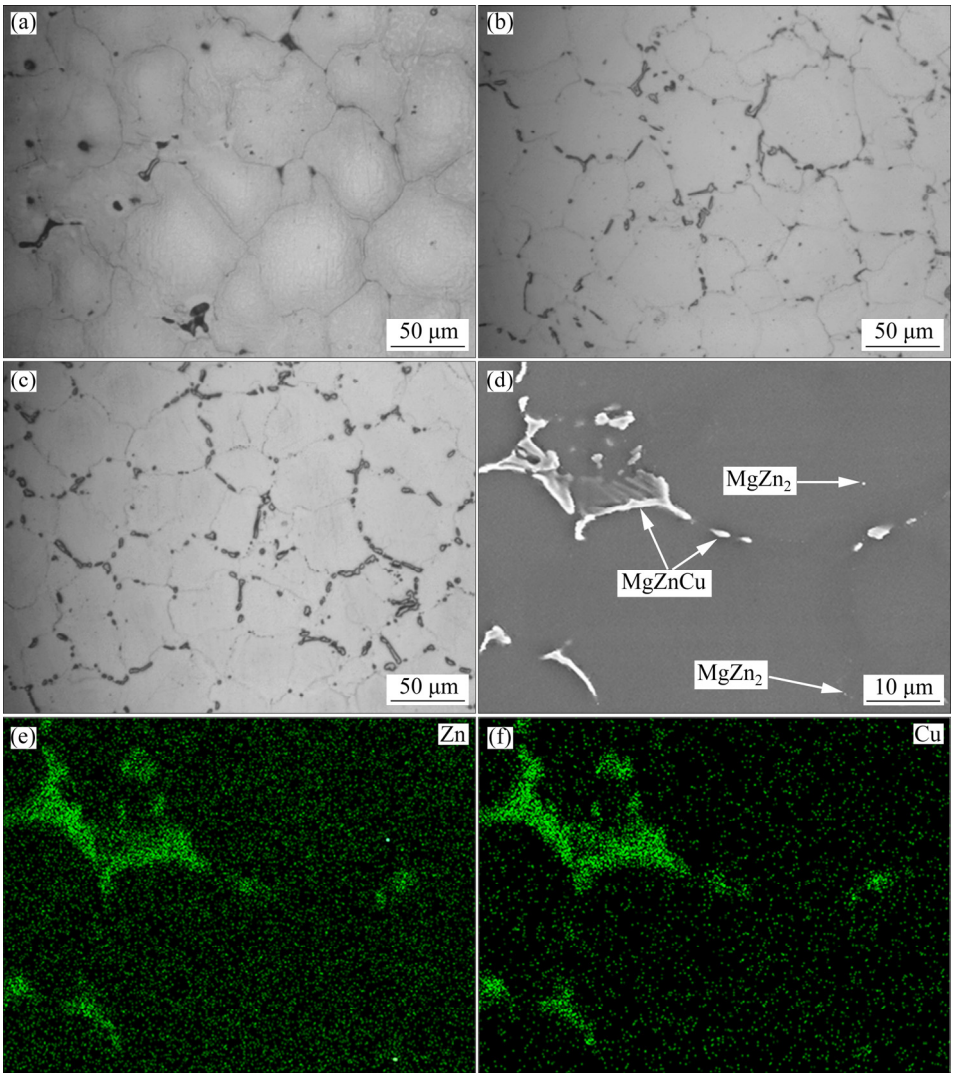

Fig. 3 Optical microstructures of as-homogenized ZK60 (a), ZK60+0.5Cu (b) and ZK60+1.0Cu (c), SEM image (d) and corresponding EDS elemental mappings of Zn (e) and Cu (f) of as-homogenized ZK60+1.0Cu alloy

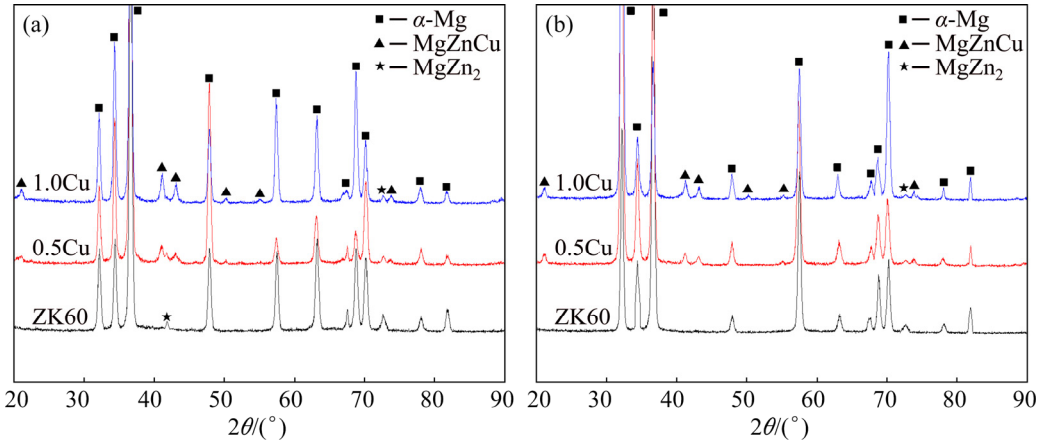

Fig. 4 XRD patterns of as-cast (a) and as-homogenized (b) alloys

phase increases and that of $MgZn_2$ phase decreases with increasing Cu addition. This can be ascribed to the low solubility of Cu in the α-Mg matrix (0.31−0.55 wt.% in pure Mg at 400 °C [32]). After solid solution treatment, the peak intensity of $MgZn_2$ phase sharply decreases while no obvious change is observed in MgZnCu phase (Fig. 4(b)).

3.2 Microstructural characteristics and texture evolution of ES alloys

The optical micrographs of ES ZK60+0.5Cu alloy at the die corner are shown in Fig. 5. The relationship of equivalent strains (ε) in Regions 1, 2, and 3 is $\varepsilon_1 \approx \varepsilon_2 < \varepsilon_3$, as shown in Fig. 5(a). A large equivalent strain is the main factor of fine and uniform microstructure observed in the ES alloy. So, the typical bimodal structure consisting of long serrated unDRX grains and veined ultrafine DRX grains not observed in Region 3 is reasonable. Our previous study showed that the difference in microstructures at Regions 1 and 2 with approximately equivalent strains owing to the $\{10\bar{1}2\}$ extension twinning forming in Region 1 could act as the nucleation site of DRX [33]. This shows the diverse effect of different regions at the die corner on DRX and Region 3 with the optimal grain refining effect.

Figure 6 shows the microstructures of ES alloys. Grain refinement can be observed after ES, and the DRX grain size first decreases and then increases. The volume fraction of bimodal structure in the forming area decreases compared with the extrusion area. This shows that DRX is sensitive to the die corner, where the extra shear forces further induce DRX.

In the forming area, the EDS results show that the extrusion streamline is composed of a broken $MgZn_2$ phase parallel to ED in the Cu-free alloy (Fig. 7(a)). The irregular block-shaped and strip-shaped MgZnCu phase is mainly distributed in DRX area in the Cu-added alloys; a spot of spherical-shaped particles with a size of ~500 nm can be observed to be $MgZn_2$ phases (Figs. 7(b, c)). The high interfacial energy between MgZnCu phase and α-Mg matrix increases the stress accumulation during plastic deformation [34], thus increasing the contribution of PSN to the DRX.

Figure 8 shows the TEM images of ES ZK60+1.0Cu alloy in the forming area. According to the results of diffraction spots analysis (Fig. 8(a)), the MgZnCu phase has a cubic structure, and the lattice parameter is 0.71. Meanwhile, a large stress accumulation around hard MgZnCu phase induces dislocation climb, accounting for the dislocation pile-up (as indicated by red ellipse in Fig. 8(a)). The dispersely distributed nanosized $MgZn_2$ precipitates within grains interior are characterized by selected area electron diffraction (SAED), exhibiting strong pinning effect of dislocation movement (as indicated in Fig. 8(b)). Sub-boundaries are

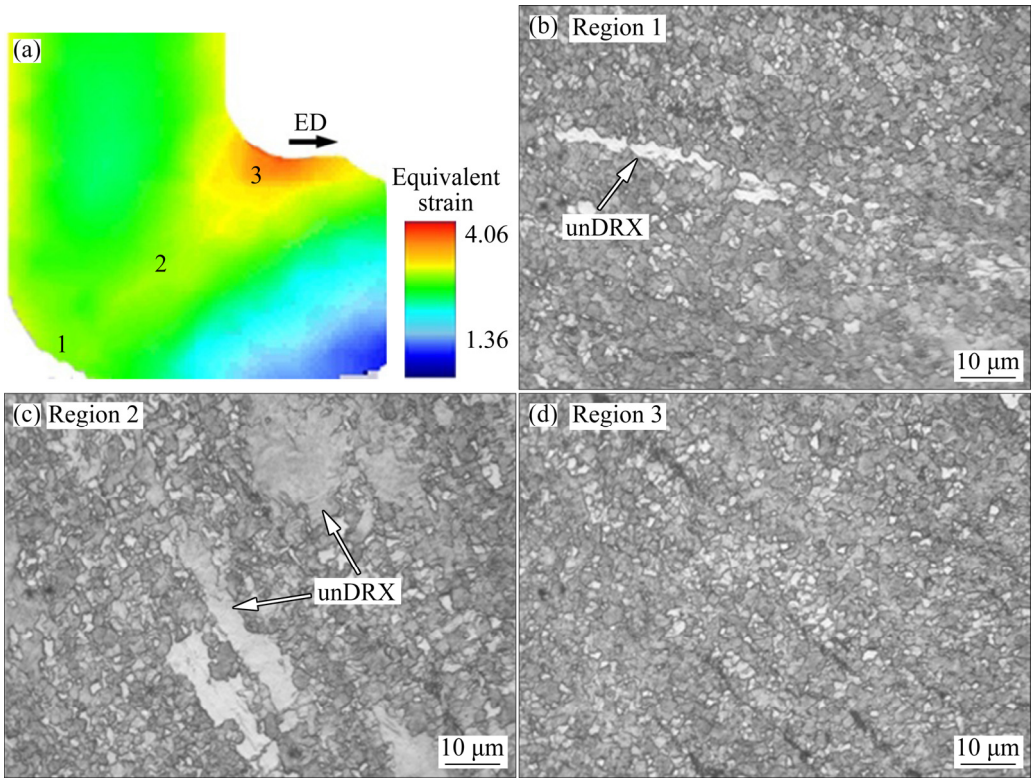

Fig. 5 Schematic diagram of equivalent strain obtained using DEFORMT M-3D software (a) and optical microstructures of ZK60+0.5Cu alloy in die corner (b−d)

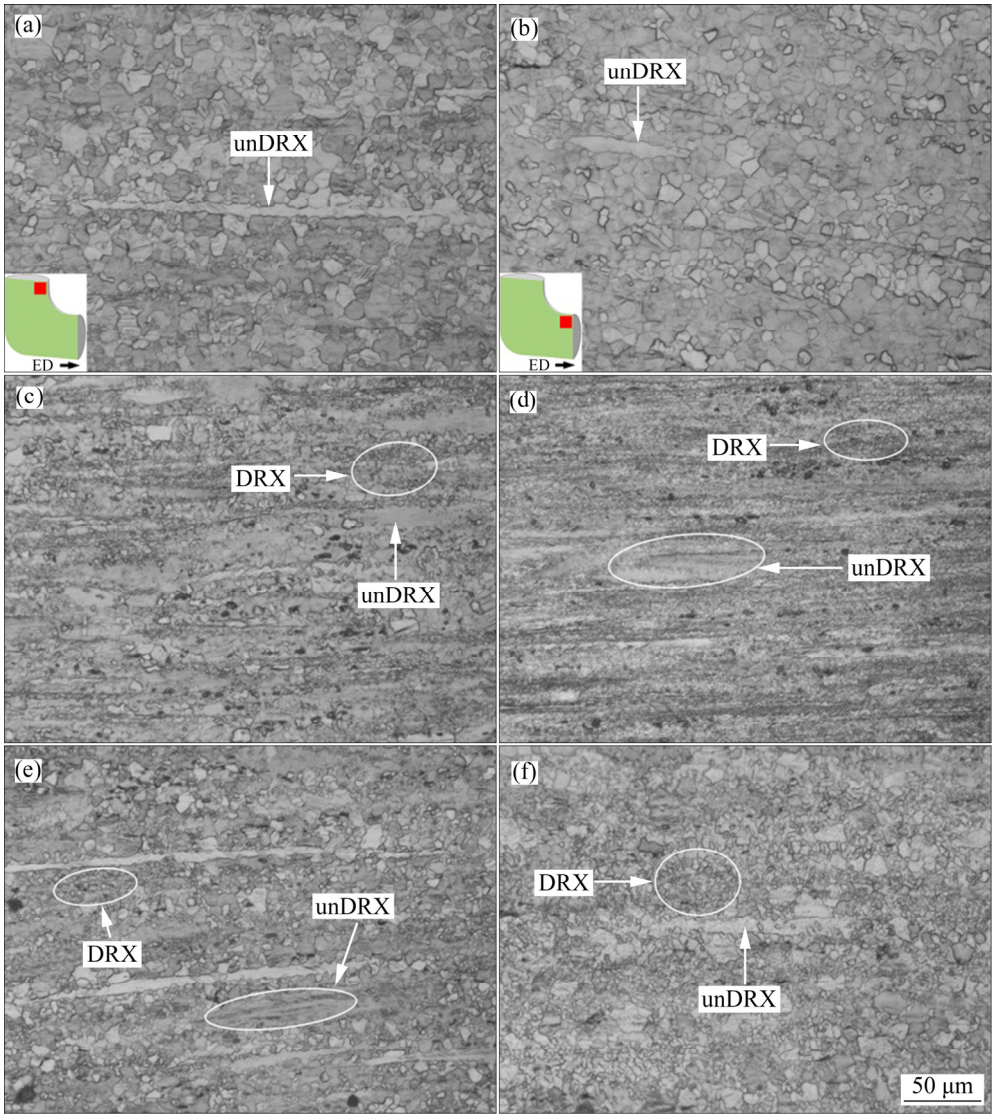

Fig. 6 Optical microstructures of ES alloys in extrusion area (a, c, e) and in forming area (b, d, f): (a, b) ZK60; (c, d) ZK60+0.5Cu; (e, f) ZK60+1.0Cu

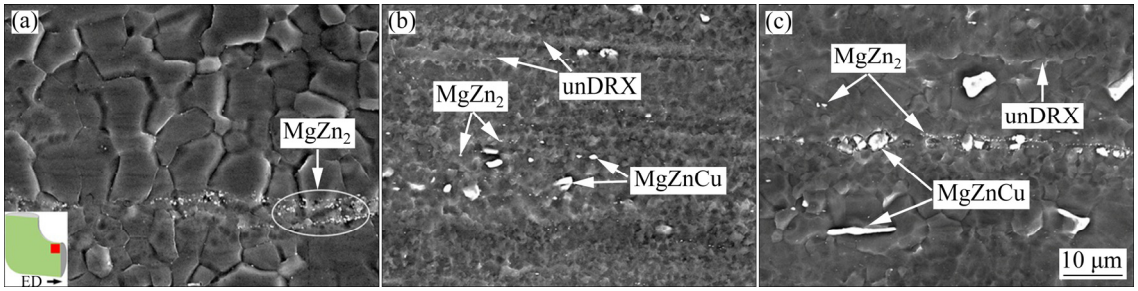

Fig. 7 SEM images of ES ZK60 (a), ZK60+0.5Cu (b) and ZK60+1.0Cu (c) alloys in forming areas

observed in adjacent DRX grains (as indicated by red arrow in Fig. 8(c)). MgZnCu phases aligned along the triangular sub-boundaries can act as effective pinning obstacles against fine DRX grain growth at elevated temperatures (Fig. 8(c)), conducive to obtain ultrafine grain alloy in ES.

Figure 9 shows EBSD results (perpendicular to the ED) for a comparative analysis of inverse pole figure orientation maps (IPF-Y), microtexture, and variations in the average grain size of ES alloys in the extrusion and forming areas. The average grain sizes of ZK60, ZK60+0.5Cu, and ZK60+1.0Cu

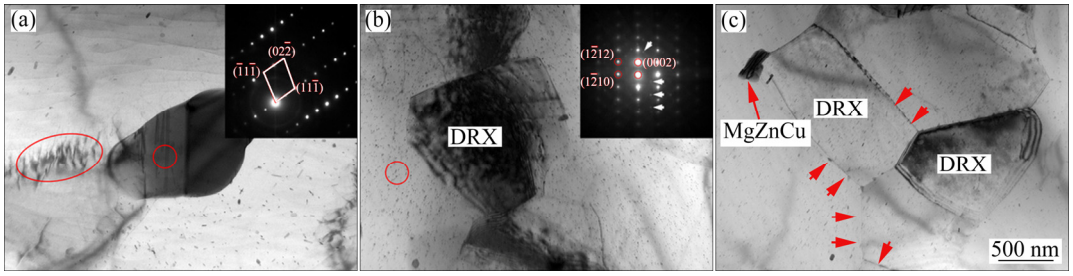

Fig. 8 Representative TEM images of ES ZK60+1.0Cu alloy in forming area

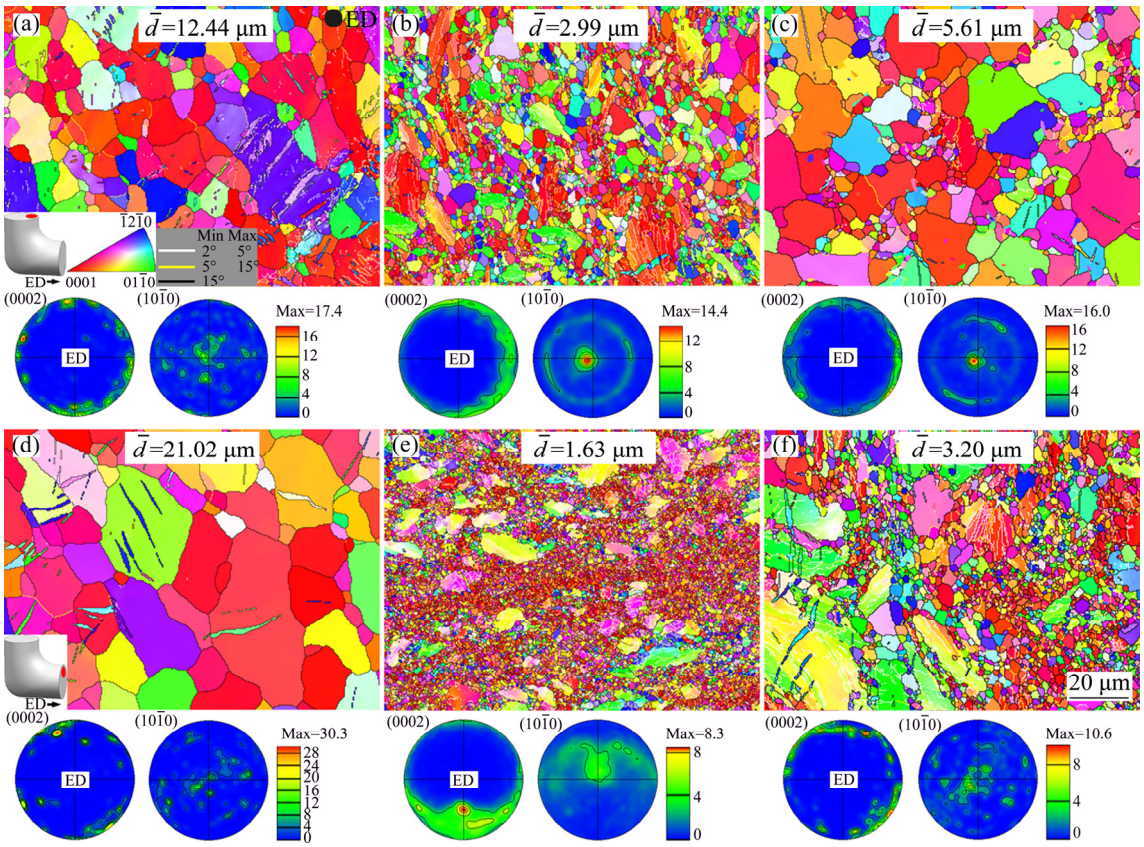

Fig. 9 EBSD results including IPF-Y, (0002) and $(10\bar{1}0)$ pole figures in extrusion (a−c) and forming (d−f) areas: (a, d) ZK60; (b, e) ZK60+0.5Cu; (c, f) ZK60+1.0Cu

alloys in the extrusion and forming areas are 12.44, 2.99 and 5.61 μm; 21.02, 1.63 and 3.20 μm, respectively. The actual temperature increases by ~50 °C near the die corner under the joint action of deformation heat and friction heat generated during ES, resulting in the growth of DRX grains in the extrusion area [35]. The variation in average grain size during ES is related to the degree of DRX grain growth and recrystallization of initial coarse unDRX grains in the extrusion area. The MgZnCu phase distributed at triangular sub-boundaries can act as a barrier to the migration of DRX grain boundaries, and the extra shear forces in die corner further strengthen PSN effect induced by hard MgZnCu phase compared to conventional forward extrusion. On the other hand, the grain refinement of Cu-added alloys can be ascribed to an increase in the volume fraction of grain boundaries in the ingot that can also act as nucleation sites for DRX [36]. Therefore, coarser DRX grains of ES alloy are observed in the forming areas than in extrusion areas, especially for ZK60 alloy, and the average grain size of Cu-added alloys in the forming area is less than that in extrusion area. A few $\{10\bar{1}2\}$ tension twins with misorientation angle of ~86° from parent grain are clearly observed in the alloys (Figs. 9(a–d, f)). Further DRX existing in the Cu-added alloys depends on the orientation maps

observation and the reduced maximum intensities of ED pole figures in the forming area. In fact, it has been reported that the occurrence of further DRX is accompanied with a weaker texture of extruded Mg alloy [37,38]. The maximum intensities of texture of ZK60, ZK60+0.5Cu, and Zk60+1.0Cu alloys in the extrusion and forming areas are 17.4, 14.4 and 16.0; 30.3, 8.3 and 10.6, respectively. Furthermore, the significant DRX of ZK60+0.5Cu alloys obtained via ES can be confirmed based on reduced maximum intensities (as indicated by pole figures in Figs. 9(b, e)). Basal poles of most grains nearly perpendicular to the ED in the extrusion area are also observed, and the Cu-added alloys exhibit typical basal fiber texture (as indicated by pole figures in Figs. 9(b, c)). Compared to the extrusion area, the angle between basal poles of most grains and ED changes to some extent, and the basal fiber texture of ZK60+0.5Cu alloy in the forming area disappears, with basal poles tilting away from the ED by ~45°(as indicated by pole figures in Fig. 9(e)).

The distribution of Schmid factor for $\{0001\}\langle 11\bar{2}0\rangle$ basal slip during tensile test at ambient temperature along ED is shown in Fig. 10. In the extrusion area, the distributions of Schmid

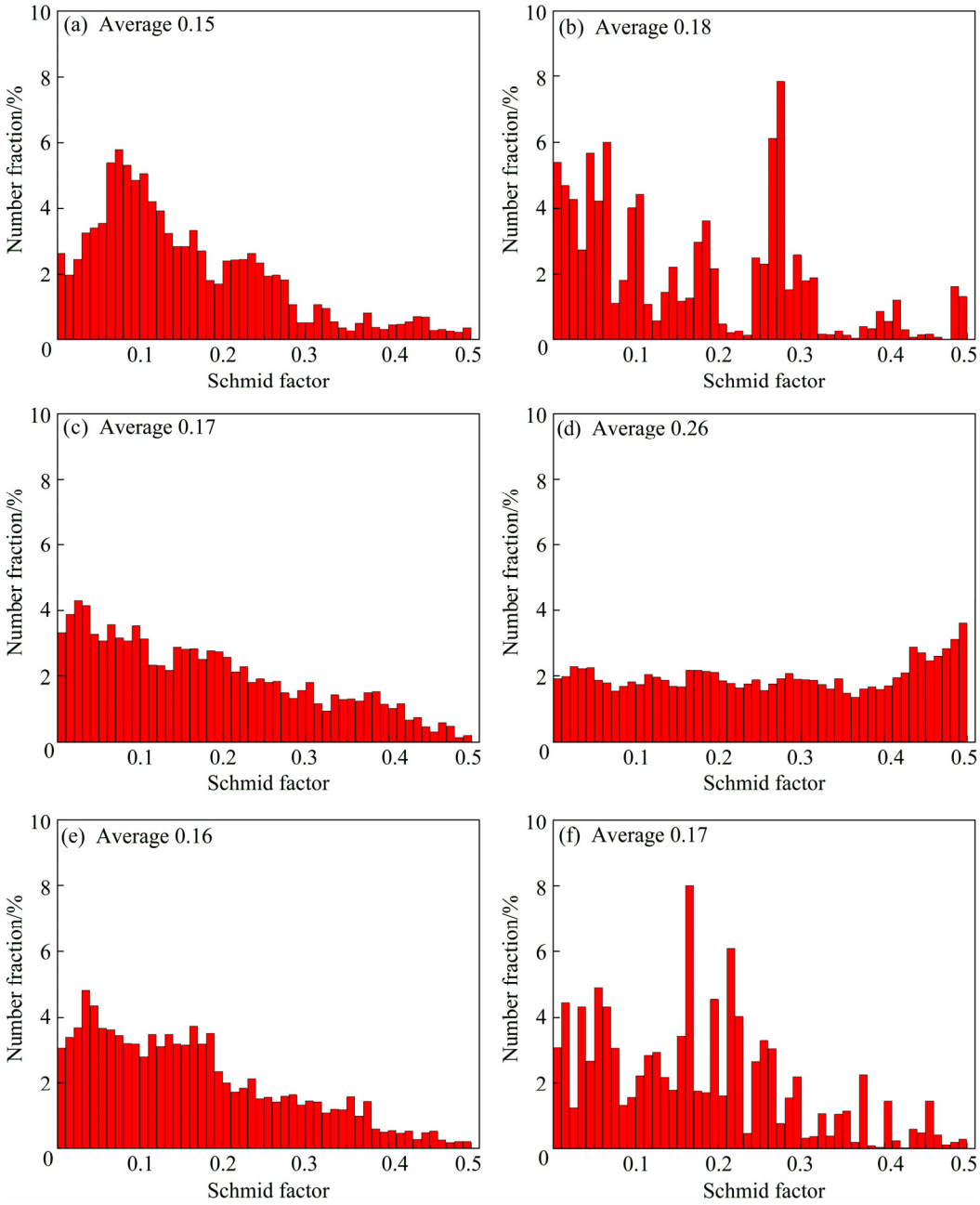

Fig. 10 Distribution of Schmid factor for basal slip of alloys in extrusion (a, c, e) and forming (b, d, f) areas: (a, b) ES ZK60; (c, d) ZK60+0.5Cu; (e, f) ZK60+1.0Cu

factor are mainly concentrated between 0 and 0.2 (Figs. 10(a, c, e)), where the average Schmid factors of ZK60, ZK60+0.5Cu, and ZK60+1.0Cu are 0.15, 0.17 and 0.16, respectively. The proportions of Schmid factor between 0.2 and 0.5 increase to some extent for the alloys in the forming area (Figs. 10(b, d, f)), particularly for ZK60+0.5Cu. The corresponding average Schmid factor even reaches up to 0.26. The basal slip is a dominant deformation mode after yield point during the tensile test conducted at room temperature of Mg alloy; in general, a high Schmid factor induces better plasticity [39].

3.3 Mechanical properties of ES alloys

Figure 11 shows the mechanical properties of ES alloys in the forming area, including ultimate tensile strength (UTS), yield strength (YS) and elongation to failure (δ). The addition of Cu remarkably improves the strength of alloys, and the optimal strength−ductility combination of ZK60+0.5Cu alloy (UTS of 396 MPa, YS of 313 MPa, and δ of 20.3%) is mainly dependent on the finest DRX grains of 1.63 μm and the largest Schmid factor for basal slip of 0.26. The grain size is crucial for the mechanical properties of extruded Mg alloys in view of other strengthening mechanisms due to the high value of slope k_y in the Hall−Petch formula [40]. Normally, The ZK60 alloy with a large grain size should possess inferior strength compared to this study because of strong texture hardening effect and precipitation strengthening induced by substantial $MgZn_2$ precipitates during ES. The excessive Cu addition decreases ductility compared to ZK60 alloy, indicating that hard MgZnCu phase can cause a variation in the fracture mode of ZK60+1.0Cu alloy.

The microvoids and tensile fracture surfaces of ES ZK60 and ZK60+1.0Cu alloys in the forming area are shown in Fig. 12. A distinct increase in the number of dimples is observed with Cu addition,

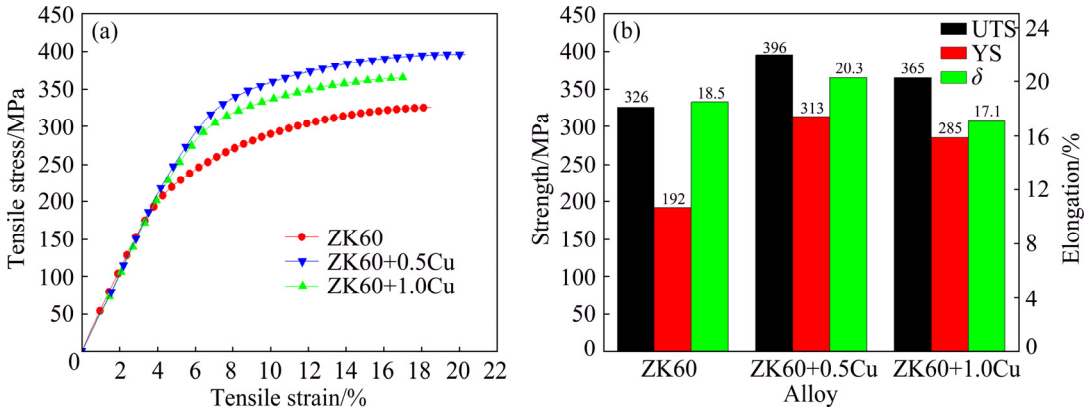

Fig. 11 Stress−strain curves (a) and tensile properties (b) of ES alloys in forming areas

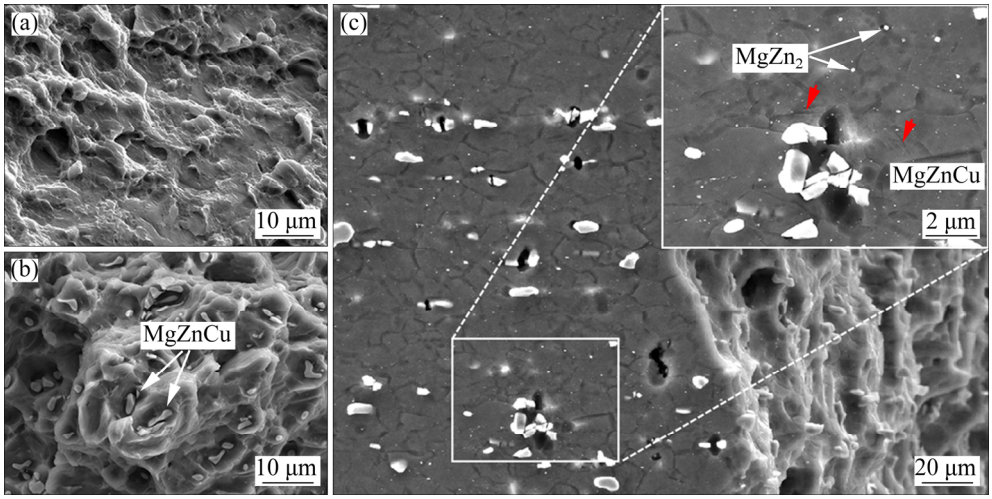

Fig. 12 SEM images of tensile fracture surface (a, b) and microstructure of ES alloys in forming area (c): (a) ZK60; (b, c) ZK60+1.0Cu

as similarly observed in the cleavage planes (Figs. 12(a, b)). This indicates that the fracture mode varies from quasi-cleavage to ductile type. Furthermore, large MgZnCu phases located at deep dimples are also observed (Fig. 12(b)). A great deal of microvoids formed around MgZnCu phase, and fine spherical $MgZn_2$ aligned at grain boundaries are observed in ZK60+1.0Cu alloy (Fig. 12(c)), confirming that severe stress accumulation caused by hard MgZnCu phase can act as the nucleation sites of microcracks when the Cu-added alloy is subjected to tensile test at ambient temperature. This observation well explains that the tensile elongation of ZK60+1.0Cu alloy is less than that of ZK60 alloy. Some previous studies [41,42] reported that $\{10\bar{1}1\}$ contraction twins and $\{10\bar{1}1\}-\{10\bar{1}2\}$ double twins formed within large DRX grain interior could also act as microcrack sources of extruded Mg−Al−Zn alloy under tensile loading along ED. Herein, the type of twins observed near microcrack is still not clear (as indicated by red arrow in Fig. 12(c)), which needs further investigation in the future.

4 Conclusions

(1) The main phase composition is converted from α-Mg and $MgZn_2$ phases to α-Mg, $MgZn_2$ and MgZnCu phases with the addition of Cu to ZK60 alloy. With the increase in Cu content, the volume fraction of MgZnCu phase gradually increases. For the as-homogenized alloy, most $MgZn_2$ phases are dissolved in the α-Mg matrix, but not in the MgZnCu phases.

(2) The hard MgZnCu phase observed can strengthen PSN effect that further induces the DRX of ES Cu-added alloys, and the extra shear forces caused by die corner can also promote DRX. Adversely, the high temperature generated from die corner under the joint action of deformation heat and friction heat accounts for the growth of DRX grains; however, the MgZnCu phases distributing along the triangular DRX grain boundaries act as obstacles for the migration of grain boundaries, in favor of obtaining ultrafine grain alloys.

(3) The ES ZK60+0.5Cu alloy has the optimal strength−ductility combination (UTS of 396 MPa, YS of 313 MPa, and δ of 20.3%), which can be ascribed to strong grain boundary strengthening and high Schmid factor for basal slip. In addition, decrease in ductility is related to the aggregation of microvoids around the hard MgZnCu phase of excessive Cu-added alloy.

References

[1] KULEKCI M K. Magnesium and its alloys applications in automotive industry [J]. International Journal of Advanced Manufacturing Technology, 2009, 39: 851−865.

[2] LIN C Y, BOR H Y, CHAO C G, LIU T F. Enhanced ductility of the ZA85 magnesium alloy fabricated by equal-channel angular pressing [J]. Journal of Alloys and Compounds, 2013, 556: 26−31.

[3] XIONG Jiang-ying, CHEN Zhi-yong, YI Li, HU Shao-hua, CHEN Tao, LIU Chu-ming. Microstructure and mechanical properties of annealed Mg−0.6wt.%Zr sheets by unidirectional and cross rolling [J]. Materials Science and Engineering A, 2014, 590: 60−65.

[4] YANG Ming-bo, PAN Fu-sheng. Comparative studies on as-cast microstructures and mechanical properties between Mg−3Ce−1.2Mn−0.9Sc and Mg−3Ce−1.2Mn−1Zn magnesium alloys [J]. Transactions of Nonferrous Metals Society of China, 2012, 22: 53−59.

[5] XU C, NAKATA T, FAN G H, LI X W, TANG G Z, GENG L, KAMADO S. Microstructure and mechanical properties of extruded Mg−Gd−Y−Zn alloy with Mn or Zr addition [J]. Journal of Materials Science, 2019, 54: 10473−10488.

[6] PARK S H, JUNG J G, KIM Y M, YOU B S. A new high-strength extruded Mg−8Al−4Sn−2Zn alloy [J]. Materials Letters, 2015, 139: 35−38.

[7] RAO K P, IP H Y, SURESH K, PRASAD Y V R K, WU C M L, HORT N, KAINER K U. Compressive strength and hot deformation mechanisms in as-cast Mg−4Al−2Ba−2Ca (ABaX422) alloy [J]. Philosophical Magazine, 2013, 93: 4364−4377.

[8] JIA Qing-gong, ZHANG Wen-xin, SUN Yi, XU Chun-xiang, ZHANG Jin-shan, KUAN Jun. Microstructure and mechanical properties of as-cast and extruded biomedical Mg−Zn−Y−Zr−Ca alloy at different temperatures [J]. Transactions of the Nonferrous Metals Society of China, 2019, 29: 515−525.

[9] LIU Jin-xue, LIU Ke, LI Shu-bo, WANG Zhao-hui, DU Wen-bo. Microstructure evolution of the Mg−3Zn−0.5Er alloy during hot rolling [J]. Materials Science Forum, 2017, 898: 118−123.

[10] SANJARI M, KABIR A S H, FARZADFAR A, UTSUNOMIYA H, JUNG I H, PETROV R, KESTENS L, YUE S. Promotion of texture weakening in magnesium by alloying and thermomechanical processing: (I) Alloying [J]. Journal of Materials Science, 2014, 49: 1408−1425.

[11] JIANG Jing, BI Guang-li, WANG Guo-yong, JIANG Qing, LIAN Jian-she, JIANG Zhong-hao. Strain-hardening and warm deformation behaviors of extruded Mg−Sn−Yb alloy sheet [J]. Journal of Magnesium and Alloys, 2014, 2: 116−123.

[12] ZHANG Yang, CHEN Xiao-yang, LU Ya-lin, LI Xiao-ping. Microstructure and mechanical properties of as-extruded Mg−Sn−Zn−Ca alloy with different extrusion ratios [J].

Transactions of Nonferrous Metals Society of China, 2018, 28: 2190−2198.

[13] ZHANG Bao-ping, WANG Yin, GENG Lin, LU Chun-xiang. Effects of calcium on texture and mechanical properties of hot-extruded Mg−Zn−Ca alloys [J]. Materials Science and Engineering A, 2012, 539: 56−60.

[14] YU Kun, RUI Shou-tai, WANG Xiao-yan, WANG Ri-chu, LI Wen-xian. Texture evolution of extruded AZ31 magnesium alloy sheets [J]. Transactions of the Nonferrous Metals Society of China, 2009, 19: 511−516.

[15] PAN Fu-sheng, MAO Jian-jun, ZHANG Gen, TANG Ai-tao, SHE Jia. Development of high-strength, low-cost wrought Mg−2.0mass%Zn alloy with high Mn content [J]. Progress in Natural Science: Materials International, 2016, 26: 630−635.

[16] GUO Kun-yu, XU Chang, LIN Xiao-ping, YE Jie, ZHANG Chong, HUANG Duo. Microstructure and strengthening mechanism of Mg−5.88Zn−0.53Cu−0.16Zr alloy solidified under high pressure [J]. Transactions of Nonferrous Metals Society of China, 2020, 30: 99−109.

[17] ZHU H M, SHA G, LIU J W, WU C L, LUO C P, LIU Z W, ZHENG R K, RINGER S P. Microstructure and mechanical properties of Mg−6Zn−*x*Cu−0.6Zr (wt.%) alloys [J]. Journal of Alloys and Compounds, 2011, 509: 3526−3531.

[18] WANG Zhi, ZHOU Le, LI Yi-zhou, WANG Feng, LIU Zheng, MAO Ping-li, JIANG Xiao-ping. Hot tearing behaviors and in-situ thermal analysis of Mg−7Zn−*x*Cu−0.6Zr alloys [J]. Transactions of Nonferrous Metals Society of China, 2018, 28: 1504−1513.

[19] CHEN Xian-hua, LIU Li-zi, PAN Fu-sheng, MAO Jian-jun, XU Xiao-yang, YAN Tao. Microstructure, electromagnetic shielding effectiveness and mechanical properties of Mg−Zn−Cu−Zr alloys [J]. Materials Science and Engineering B, 2015, 197: 67−74.

[20] GANESHAN S, SHANG S L, WANG Y, LIU Z K. Effect of alloying elements on the elastic properties of Mg from first-principles calculations [J]. Acta Materialia, 2009, 57: 3876−3884.

[21] VALLE J A D, CARRE O F, RUANO O A. Influence of texture and grain size on work hardening and ductility in magnesium-based alloys processed by ECAP and rolling [J]. Acta Materialia, 2006, 54: 4247−4259.

[22] PARK S S, YOU B S, YOON D J. Effect of the extrusion conditions on the texture and mechanical properties of indirect-extruded Mg−3Al−1Zn alloy [J]. Journal of Materials Processing Technology, 2009, 209: 5940−5943.

[23] YING Tao, HUANG Jian-ping, ZHENG Ming-yi, WU Kun. Influence of secondary extrusion on microstructures and mechanical properties of ZK60 Mg alloy processed by extrusion and ECAP [J]. Transactions of Nonferrous Metals Society of China, 2012, 22: 1896−1901.

[24] CHENG Wei-li, TIAN Liang, WANG Hong-xia, BIAN Li-ping, Yu Hui. Improved tensile properties of an equal channel angular pressed (ECAPed) Mg−8Sn−6Zn−2Al alloy by prior aging treatment [J]. Materials Science and Engineering A, 2017, 687: 148−154.

[25] DUMITRU F D, HIGUERA-COBOS O F, CABRERA J M. ZK60 alloy processed by ECAP: Microstructural, physical and mechanical characterization [J]. Materials Science and Engineering A, 2014, 594: 32−39.

[26] KIM W J, AN C W, KIM Y S, HONG S I. Mechanical properties and microstructures of an AZ61 Mg alloy produced by equal channel angular pressing [J]. Scripta Materialia, 2002, 47: 39−44.

[27] ZHANG Ding-fei, HU Hong-jun, PAN Fu-sheng, YANG Ming-bo, ZHANG Jun-ping. Numerical and physical simulation of new SPD method combining extrusion and equal channel angular pressing for AZ31 magnesium alloy [J]. Transactions of Nonferrous Metals Society of China, 2010, 20: 478−483.

[28] ZHANG Jing, GUO Z X, PAN Fu-sheng, LI Zhong-sheng, LUO Xiao-dong. Effect of composition on the microstructure and mechanical properties of Mg−Zn−Al alloys [J]. Materials Science and Engineering A, 2007, 456: 43−51.

[29] LI Han, DU Wen-bo, LI Shu-bo, WANG Zhao-hui. Effect of Zn/Er weight ratio on phase formation and mechanical properties of as-cast Mg−Zn−Er alloys [J]. Materials and Design, 2012, 35: 259−265.

[30] DING Zhi-bing, ZHAO Yu-hong, LU Ruo-peng, YUAN Mei-ni, WANG Zhi-jun, LI Hui-jun, HOU Hua. Effect of Zn addition on microstructure and mechanical properties of cast Mg−Gd−Y−Zr alloys [J]. Transactions of Nonferrous Metals Society of China, 2019, 29: 722−734.

[31] WU Meng-meng, WEN Li, TANG Bi-yu, PENG Li-ming, DING Wen-jiang. First-principles study of elastic and electronic properties of $MgZn_2$ and $ScZn_2$ phases in Mg−Sc−Zn alloy [J]. Journal of Alloys and Compounds, 2010, 506: 412−417.

[32] BUHA J, OHKUBO T. Natural aging in Mg−Zn(−Cu) alloys [J]. Metallurgical and Materials Transactions A, 2008, 39: 2259−2273.

[33] DAI Shuai, WANG Feng, WANG Zhi, LIU Zheng, MAO Ping-li. Microstructure, mechanical properties, and texture evolution of Mg−Zn−Y−Zr alloy fabricated by hot extrusion–shearing process [J]. Journal of Materials Science, 2020, 55: 375−388.

[34] WANG Yong-jian, PENG Jian, ZHONG Li-ping. On the microstructure and mechanical property of as-extruded Mg−Sn−Zn alloy with Cu addition [J]. Journal of Alloys and Compounds, 2018, 744: 234−242.

[35] JUNG J G, PARK S H, YOU B S. Effect of aging prior to extrusion on the microstructure and mechanical properties of Mg−7Sn−1Al−1Zn alloy [J]. Journal of Alloys and Compounds, 2015, 627: 324−332.

[36] JIANG M G, XU C, NAKATA T, YAN H, CHEN R S, KAMADO S. Development of dilute Mg−Zn−Ca−Mn alloy with high performance via extrusion [J]. Journal of Alloys and Compounds, 2016, 668: 13−21.

[37] STANFORD N, ATWELL D, BEER A, DAVIES C, BARNETT M R. Effect of microalloying with rare-earth elements on the texture of extruded magnesium-based alloys [J]. Scripta Materialia, 2008, 59: 772−775.

[38] LI R G, NIE J F, HUANG G J, XIN Y C, LIU, Q. Development of high-strength magnesium alloys via combined processes of extrusion, rolling and ageing [J]. Scripta Materialia, 2011, 64: 950−953.

[39] YAN H, XU S W , CHEN R S, KAMADO S, HONMA T, HAN E H. Activation of $\{10\bar{1}2\}$ twinning and slip in high

ductile Mg−2.0Zn−0.8Gd rolled sheet with non-basal texture during tensile deformation at room temperature [J]. Journal of Alloys and Compounds, 2013, 566: 98−107.

[40] YUAN W, PANIGRAHI S K, SU J Q, MISHRA R S. Influence of grain size and texture on Hall−Petch relationship for a magnesium alloy [J]. Scripta Materialia, 2011, 65: 994−997.

[41] BARNETT M R. Twinning and the ductility of magnesium alloys: Part II. “Contraction” twins [J]. Materials Science and Engineering A, 2007, 464: 8−16.

[42] ANDO D, KOIKE J, SUTOU Y. Relationship between deformation twinning and surface step formation in AZ31 magnesium alloys [J]. Acta Materialia, 2010, 58: 4316−4324.

Cu 对挤压剪切 ZK60 合金显微组织、力学性能及织构演变的影响

代 帅[1,2]，王 峰[1,2]，王 志[1,2]，刘 正[1,2]，毛萍莉[1,2]

1. 沈阳工业大学 材料科学与工程学院，沈阳 110870；
2. 辽宁省镁合金及成形技术重点实验室，沈阳 110870

摘 要：采用金属型铸造方法制备 Mg−6Zn−*x*Cu−0.6Zr(*x*=0，0.5，1.0)(质量分数，%)合金，并对其进行均匀化热处理与挤压剪切成形。采用 OM、SEM/EDS、XRD、TEM、EBSD 及拉伸试验研究合金的显微组织及力学性能。结果表明：在挤压剪切过程中，硬质相 MgZnCu 能够增强粒子激发形核(PSN)效应及阻碍高温下动态再结晶(DRX)晶界的迁移。挤压剪切 ZK60+0.5Cu 合金具有最优的强度−塑性组合(抗拉强度 396 MPa、屈服强度 313 MPa 和伸长率 20.3%)，这归因于强烈的晶界强化及{0001}⟨$11\bar{2}0$⟩基面 Schmid 因子的提高。相比于 ZK60 合金，ZK60+1.0Cu 合金伸长率的降低与 MgZnCu 相引起的微孔聚集有关。

关键词：Mg−Zn−Cu−Zr 合金；挤压剪切工艺；显微组织表征；力学性能；织构演变；强化机制

(Edited by Bing YANG)